Journal of Materials Chemistry A

ROYAL SOCIETY OF CHEMISTRY

PAPER

View Article Online
View Journal | View Issue

Check for updates

Cite this: J. Mater. Chem. A, 2023, 11, 10669

Holistic functional biomimetics: a key to make an efficient electrocatalyst for water oxidation†

Lizhou Fan,[a] Yuxiang Song,[d] Fan Zhang,[b] Brian J. J. Timmer,[a] Alexander Kravberg,[a] Biaobiao Zhang *[ad] and Licheng Sun[acd]

Water oxidation is the holy grail reaction of natural and artificial photosynthesis. How to design an efficient water-oxidation catalyst remains a long-term challenge for solar fuel production. The rate of water oxidation in photosystem II by the oxygen-evolving complex (OEC) Mn_4CaO_5 cluster is as high as 100–400 s^{-1}. Mimicking the structures of the OEC is a straightforward strategy to design water-oxidation catalysts. However, the high efficiency of the OEC relies on not only its highly active site but also its holistic system for well-organized electron transfer and proton transport. Lacking such a holistic functional system makes δ-MnO_2 a poor water-oxidation catalyst, although the local structure of δ-MnO_2 is similar to that of the Mn_4CaO_5 cluster. Electrocatalysts simultaneously imitating the catalytically active sites, fast electron transfer, and promoted proton transport in a natural OEC have been rarely reported. The significance of the synergy of a holistic system is underrated in the design of water-oxidation catalysts. In this work, we fabricated holistic functional biomimetic composites of two-dimensional manganese oxide nanosheets and pyridyl-modified graphene (MnO_x-NS/py-G) for electrocatalytic water oxidation. MnO_x-NS/py-G simultaneously imitates the synergy of catalytically active sites, fast electron transfer, and promoted proton transport in a natural OEC, resulting in overall 600 times higher activity than that of typical δ-MnO_2. This work demonstrates the significance of holistic functional biomimetic design and guides the development of highly active electrocatalysts for small molecule activation related to solar energy storage.

Received 19th February 2023
Accepted 19th April 2023

DOI: 10.1039/d3ta01040f

rsc.li/materials-a

Open Access Article. Published on 20 kwietnia 2023. Downloaded on 29.01.2026 18:22:29.
This article is licensed under a Creative Commons Attribution-NonCommercial 3.0 Unported Licence.

Introduction

The development of efficient water-oxidation catalysts is of significance to realize high-performance artificial photosynthesis for solar energy conversion and fuel production.[1,2] In photosystem II (PSII), water is oxidized by the oxygen-evolving complex (OEC), a Mn_4CaO_5 cluster surrounded by amino acid residues, two Cl^- ions, and many H_2O molecules.[3–5] The Mn_4CaO_5 cluster, which can be regarded as a nanosized Mn oxide in a protein environment, catalyzes water oxidation with a low overpotential of around 160 mV and a high rate of 100–400 s^{-1}.[6] Mimicking the structure of the OEC in PSII is a straightforward strategy to design water-oxidation catalysts.[2,7] A successful example is the introduction of carboxylic groups into molecular catalysts, leading to the breakthrough of water oxidation performance.[8] However, the structural similarity to the natural OEC structure is not always related to the catalytic performance. δ-MnO_2 possess similar structural properties to the Mn_4CaO_5 cluster in PSII, *e.g.*, the cabane-like local structure, and the mixing of Mn^{3+} and Mn^{4+} oxidation states, therefore, can be considered structural models for the OEC.[9–11] But the performance of typical δ-MnO_2 for water oxidation is poor, far less than that of natural enzymes.

The high efficiency of the OEC relies on its well-organized holistic system, which includes not only highly active sites for the formation of reactive high-valent metal-oxo and O–O bonds but also effective electron transfer pathways *via* nearby tyrosine residues[12] and proton transport channels *via* the Ca^{2+} ion,[13] namely the synergy of the catalytically active site, electron transfer, and proton transport (Scheme 1). However, δ-MnO_2 only imitates the core structure of the Mn_4CaO_5 cluster but cannot imitate the OEC's secondary environment.[9] Although its local structural unit is close to that of the Mn_4CaO_5 cluster, the water-oxidation performance of δ-MnO_2 is heavily limited due to the lacking exposure of catalytic sites and the components that facilitate electron transfer and proton transport.[10] In

[a]Department of Chemistry, KTH Royal Institute of Technology, 10044 Stockholm, Sweden. E-mail: zhangbiaobiao@westlake.edu.cn

[b]Division of Surface and Corrosion Science, KTH Royal Institute of Technology, 10044 Stockholm, Sweden

[c]State Key Laboratory of Fine Chemicals, Institute of Artificial Photosynthesis, DUT-KTH Joint Education and Research Center on Molecular Devices, Dalian University of Technology (DUT), 116024 Dalian, People's Republic of China

[d]Center of Artificial Photosynthesis for Solar Fuels and Department of Chemistry, School of Science and Research Center for Industries of the Future, Westlake University, Hangzhou 310024, Zhejiang, People's Republic of China

† Electronic supplementary information (ESI) available. See DOI: https://doi.org/10.1039/d3ta01040f

Open Access Article. Published on 20 kwietnia 2023. Downloaded on 29.01.2026 18:22:29.
This article is licensed under a Creative Commons Attribution-NonCommercial 3.0 Unported Licence.

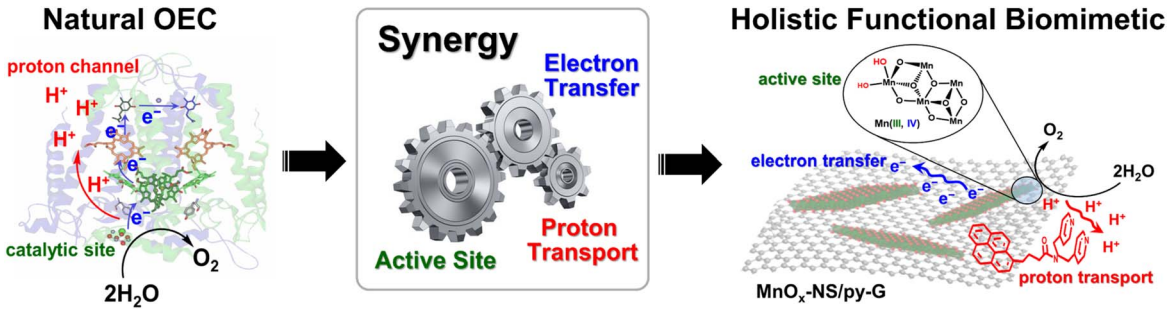

Scheme 1 Concept of holistic functional biomimetics inspired by the natural OEC's synergy of the catalytically active site, electron transfer, and proton transport.

addition to the structure of the active site, the inspiration that the design of water-oxidation catalysts can take from a natural OEC is the synergy of its holistic system.[11] To date, the significance of the synergy of a holistic system is underrated in the design of water-oxidation catalysts. Electrocatalysts simultaneously imitating the catalytically active sites, fast electron transfer, and promoted proton transport in a natural OEC have been rarely reported.

In this work, we report holistic functional biomimetic inorganic–organic composites with clearly defined structure–function relationships to display the significance of the synergy of the catalytically active site, electron transfer, and proton transport in the design of water-oxidation electrocatalysts (Scheme 1). Coordinatively unsaturated edge, corner, and defect sites on two-dimensional (2D) manganese oxide nanosheets (MnO_x-NS), which can be obtained from structural exfoliation of δ-MnO_2, serve as biomimetic active sites. To achieve fast electron transfer between local active sites, material bulk, and the electrode interface, MnO_x-NS was assembled with graphene to form a nanocomposite structure. Proton transport is essential for the formation of water-oxidation key intermediates, such as Mn^{VII}-oxo,[14] $Mn^{IV}O$,[15] and Mn^{V}-oxo.[16] Inspired by Nakamura and coworkers' study,[17] we further modified the graphene surface with pyridyl groups with a pK_a value of around 5 to accelerate proton transfer.

The fabricated holistic functional biomimetic composites of MnO_x-NS and pyridyl-modified graphene (MnO_x-NS/py-G) showed 600-fold higher catalytic activity than δ-MnO_2, being ranked on top in highly active manganese-based water-oxidation catalysts. Further in-depth studies revealed the structure–activity relationship of the MnO_x-NS/py-G composites. The activity improvement results from the synergy of sufficient exposure of catalytically active sites, fast electron transport, and efficient proton transport. Each of the factors contributes 30 times, 10 times, and 2 times to the overall activity increment, respectively. These results proved the effectiveness of the holistic functional biomimetic for electrocatalyst design.

Results and discussion

Preparation and characterization

General synthetic procedures of MnO_x-NS, MnO_x-NS/G, and MnO_x-NS/py-G are demonstrated in Scheme 2. Control samples δ-MnO_2/G and δ-MnO_2/py-G were also prepared by similar

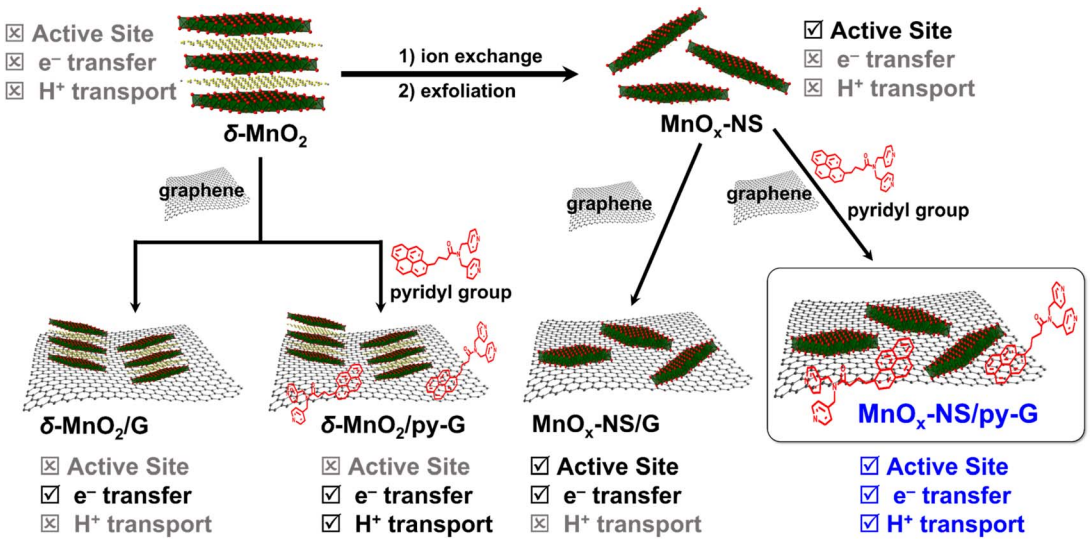

Scheme 2 Schematic illustration of the synthetic procedure of MnO_x-NS/G, MnO_x-NS/py-G, δ-MnO_2/G, and δ-MnO_2/py-G.

 This journal is © The Royal Society of Chemistry 2023

Open Access Article. Published on 20 kwietnia 2023. Downloaded on 29.01.2026 18:22:29.
This article is licensed under a Creative Commons Attribution-NonCommercial 3.0 Unported Licence.

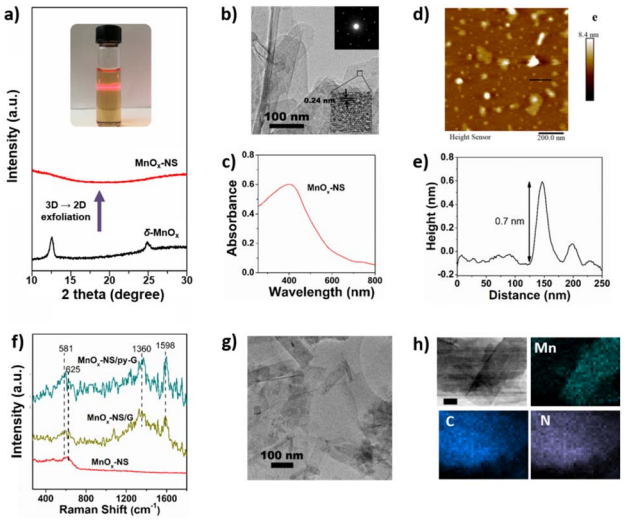

Fig. 1 (a) Optical image of the colloidal solution of exfoliated MnO_x-NS and XRD pattern of δ-MnO_2 and MnO_x-NS. (b) The TEM image of MnO_x-NS. (c) The UV-vis absorption spectra of the colloidal suspension of MnO_x-NS. (d) The AFM image and (e) the height profile of MnO_x-NS. (f) The Raman spectrum of MnO_x-NS, MnO_x-NS/G, and MnO_x-NS/py-G. (g) The TEM image of MnO_x-NS/py-G. (h) STEM-EDX elemental mapping of Mn, C, and N of MnO_x-NS/py-G (scale bar is 20 nm).

methods. The graphene used is commercial, and the pyridyl molecule for proton transport is from laboratory synthesis (Fig. S1 and S2†). A colloidal solution of 2D MnO_x-NS was first obtained from the exfoliation of δ-MnO_2 by an ion-exchange approach.[18–20] A typical Tyndall effect is observed in the brown and transparent solution under laser beam illumination, demonstrating its good dispersion and colloidal properties (inset of Fig. 1a). Fig. 1a shows the powder X-ray diffraction (XRD) spectrum of δ-MnO_2 and MnO_x-NS. In contrast to the XRD pattern of δ-MnO_2 with typical sharp peaks at $2\theta = 12.4°$, which is related to the layered structure with an interlayer spacing of 0.7 nm, the XRD spectrum of MnO_x-NS presents no diffraction peak. The disappearance of the peak at 12.4° illustrates the delamination of the long-range ordered layered structure to individual irregularly oriented nanosheets after exfoliation.[18,20]

MnO_x-NS was characterized in detail by transmission electron microscopy (TEM), ultraviolet-visible (UV-vis) spectroscopy, and atomic force microscopy (AFM). The TEM image of MnO_x-NS displays a clear single-layer nanosheet morphology (Fig. 1b). The selected area electron diffraction (SAED) pattern of MnO_x-NS exhibits hexagonally arranged diffraction spots (inset of Fig. 1b). All these results are in sharp contrast to δ-MnO_2, which exhibits a multi-layered morphology and polycrystal SAED image with diffraction rings, showing the exfoliation of a multi-layered structure to monolayer nanosheets (Fig. S3†).[20] Notably, the SAED results of δ-MnO_2 and MnO_x-NS present hexagonal reciprocal lattices, indicating that MnO_x-NS retains a similar crystalline structure to the δ-MnO_2 crystal. The HRTEM image of MnO_x-NS presents a lattice fringe with an interlayer spacing of 0.24 nm, which can be assigned to the {100} plane of δ-MnO_2.[21,22] The UV-vis spectrum of MnO_x-NS shows a broad absorption peak at around 400 nm, which can be attributed to the d–d transition of Mn ions in MnO_6 octahedra (Fig. 1c).[18,20] At last, the successful exfoliation of δ-MnO_2 to 2D MnO_x monolayer nanosheets was confirmed by AFM imaging of MnO_x-NS (Fig. 1d and e). A thickness of 0.7 nm was determined for MnO_x-NS, which is consistent with the thickness of the MnO_x monolayer.[18,20]

An apparent change of the electronic structure in MnO_x-NS compared to δ-MnO_2 is the increased ratio of Mn^{3+}/Mn^{4+} oxidation states, which was determined by X-ray photoelectron spectroscopy (XPS). δ-MnO_2 shows Mn peaks at 643.0, 642.1 eV, and 640.7 eV, which can be assigned to Mn^{4+}, Mn^{3+}, and a minimal amount of Mn^{2+}, respectively (Fig. S4a†).[23–26] Based on the peak integration, its Mn^{3+}/Mn^{4+} content ratio was calculated to be 0.44. Similar Mn 2p XPS peaks were presented for MnO_x-NS. However, the ratio of Mn^{3+}/Mn^{4+} oxidation states increased to 0.67, much larger than the 0.44 of δ-MnO_2. Moreover, the ratio of Mn–OH (531.0 eV)/Mn–O–Mn (529.7 eV) is calculated to be 0.46 for MnO_x-NS, much higher than 0.34 for δ-MnO_2 (Fig. S4b†).[23–25] In general, Mn–OH is a marker of active sites since the Mn ions with several coordinating –OH groups in the Mn_4CaO_5 cluster, usually labeled as Mn_4, are considered to be the active sites for O–O bond formation.[27] These XPS results demonstrate that abundant Mn^{3+} species and coordinatively unsaturated sites are exposed on MnO_x-NS upon 3D → 2D structural exfoliation, serving as biomimetic active sites.

Then, single-layer MnO_x-NS were assembled with graphene and pyridyl-modified graphene (py-G) to give the MnO_x-NS/G and MnO_x-NS/py-G samples. The Raman spectra of MnO_x-NS/G and MnO_x-NS/py-G are presented in Fig. 1f. Both the samples show additional scattering bands at 1360 and 1598 cm^{-1} compared with MnO_x-NS, which are the typical Raman signals of graphene.[28,29] The TEM images of MnO_x-NS/G and MnO_x-NS/py-G (Fig. 1g and S5†) and the energy dispersive spectroscopy (EDS) mapping (Fig. 1h) of MnO_x-NS/py-G display randomly distributed MnO_x-NS on the surface of graphene without apparent aggregation. A nitrogen fluorescence signal was presented in the EDS mapping of MnO_x-NS/py-G, confirming the homogeneous modification by the pyridyl molecule. The presence of the pyridyl molecule in MnO_x-NS/py-G can be further depicted by the electrochemical cyclic voltammetry (CV) study. A broad reduction wave was distinctly presented between −1.0 and −1.35 V (*vs.* Ag/AgCl) for MnO_x-NS/py-G, which is the typical redox peak of the pyridine moiety (Fig. S6†).[30,31] Overall, these above characterization studies thoroughly demonstrate the successful assembly of MnO_x-NS/py-G composites.

Electrocatalytic water oxidation

Electrocatalytic oxygen evolution reaction (OER) performances of δ-MnO_2, MnO_x-NS, MnO_x-NS/G, and MnO_x-NS/py-G were evaluated by loading on glass carbon (GC) electrodes under alkaline conditions (1 M KOH). δ-MnO_2 shows negligible activity within a wide potential range, which is consistent with the generally low OER activity characteristics of δ-MnO_2 (Fig. 2a).[32–34] MnO_x-NS displays significantly enhanced OER

Open Access Article. Published on 20 kwietnia 2023. Downloaded on 29.01.2026 18:22:29.
This article is licensed under a Creative Commons Attribution-NonCommercial 3.0 Unported Licence.

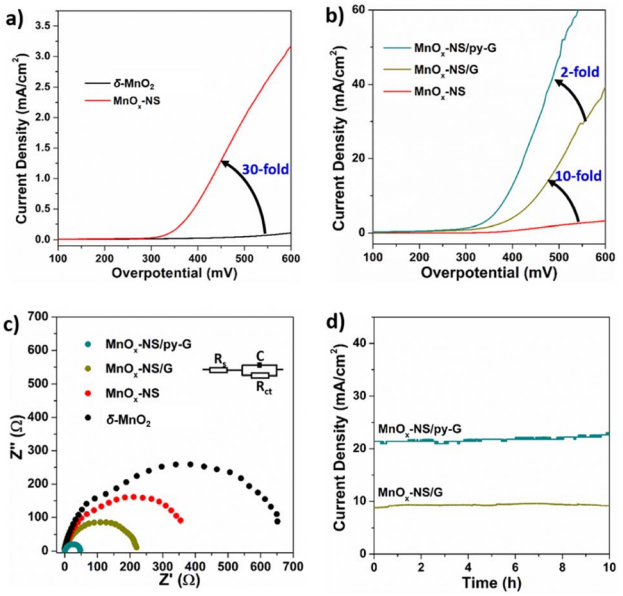

Fig. 2 (a) Polarization curves of δ-MnO_2 and MnO_x-NS. (b) Polarization curves of MnO_x-NS, MnO_x-NS/G, and MnO_x-NS/py-G. (c) Nyquist diagrams of δ-MnO_2, MnO_x-NS, MnO_x-NS/G, and MnO_x-NS/py-G. (d) Chronoamperometry curve of MnO_x-NS/G and MnO_x-NS/py-G at a 450 mV overpotential.

activity, which provides approximately 30 times higher current densities compared with δ-MnO_2 (Fig. 2a). Notably, after assembling with graphene, the catalytic current density of MnO_x-NS/G increases further by 10-fold compared to that of MnO_x-NS (Fig. 2b). Then, with the effect of the pyridyl molecule modification, 2 times improvement in OER performance was additionally achieved for the final MnO_x-NS/py-G catalyst compared to that of MnO_x-NS/G. In contrast to the initial δ-MnO_2, MnO_x-NS/py-G eventually displays 600 times higher OER activity due to the synergy of active site exposure, nanocomposite structure, and molecular modification, being ranked as a highly active manganese-based water oxidation catalyst (Fig. S7†).[35–41]

The electrochemical impedance spectroscopy (EIS) measurements under water oxidation conditions can further reflect the improved catalytic rate. MnO_x-NS/py-G exhibits a charge transfer resistance (R_{ct}) of 41.09 Ω, which is 20 times lower compared with 584.8 Ω of δ-MnO_2 (Fig. 2c). A low Tafel slope of 86 mV dec^{-1} was determined for MnO_x-NS/py-on the MnO_x-NS/py-G catalyst to assess the catalytic stability (Fig. S8†). A stable current density of 21 mA cm^{-2} was maintained during 10 h electrolysis at a 450 mV overpotential, indicating the excellent electrocatalytic durability of MnO_x-NS/py-G (Fig. 2d). However, due to the bubble removal, mass transfer, and mechanical stability problems, long-term electrolytic assessment at a large current density (*e.g.* 200 mA cm^{-2}) cannot be carried out using a GC working electrode in this study.[42] For a powder catalyst, a flow electrochemical cell and anion exchange membrane electrolyzer are better and important evaluation methods to achieve the performance of the catalyst in practical application.[42,43]

TEM, EDS-mapping, and electrochemical cyclic voltammetry of the MnO_x-NS/py-G catalyst after reaction shows comparable results with the as-synthesized catalyst, which confirm its good catalytic stability (Fig. S9 and S10†). In a separate experiment, the OER faradaic efficiency was determined to be 98% for MnO_x NS/py-G under 400 mV overpotential electrolysis, verifying that a vast majority of charges was contributed to water oxidation (Fig. S11†).

Following our design strategy in Scheme 1, the OER activities of the δ-MnO_2, MnO_x-NS, MnO_x-NS/G, and MnO_x-NS/py-G catalysts have been successively advanced owing to the directed improvement in each sample, achieving a remarkable OER performance for the final MnO_x-NS/py-G. To understand the activity enhancement from the starting inactive δ-MnO_2 to the final highly active MnO_x-NS/py-G, we then thoroughly examined the specific effects of structural exfoliation, graphene substrate assembly, and pyridyl molecule modification on electrocatalytic water oxidation.

Effects of the exposure of the active site

Compared to δ-MnO_2, the activity of MnO_x-NS increased by 30 times, indicating the significant effects of the structural exfoliation. Two possible ways may induce this dramatic improvement: (i) enlarged electrochemically active surface area (ECSA) caused by a morphology change; (ii) increased numbers of catalytic sites due to 3D → 2D structural changes. To identify the effects of structural exfoliation, we first estimated the ECSA of δ-MnO_2 and MnO_x-NS from electrochemical double-layer capacitance (C_{dl}, Fig. 3a and S12†). The linear slope of MnO_x-NS was calculated to be 0.045 mF cm^{-2}, which is only 18% higher than the 0.038 mF cm^{-2} of δ-MnO_2. The similar ECSA of δ-MnO_2 and MnO_x-NS indicates that the layered structure of δ-MnO_2 is already widely accessible for electrochemical charging, which has also been reported on double layer hydroxide materials.[44] This slight increase in ECSA contributes negligibly to the 30 times increase in activity upon exfoliation of δ-MnO_2 to MnO_x-NS.

Since the change of ECSA does not account for activity improvement, the remaining possibility is the increment of catalytic sites. Mn^{3+} species have been commonly recognized as an indicator of active sites for Mn-based water oxidation catalysts.[45,46] To investigate the promotion effect of exfoliation o active site exposure, we introduce a pyrophosphate (PP) molecule to the solution of δ-MnO_2 and MnO_x-NS, which can extract Mn^{3+} from the catalyst through coordination (Fig. 3b).[46–48] The resulting Mn^{3+}-PP species was then monitored by using the UV-vis absorption spectrum. MnO_x-NS exhibits a much higher Mn^{3+}-PP absorption peak at around 258 nm compared with δ-MnO_2. Consistent with XPS, these results demonstrate the abundance of Mn^{3+} upon exfoliation. These Mn^{3+} species can be positively involved in water oxidation as highly reactive sites, improving the catalytic activity.

With further investigations, we could propose two aspects that effectively increase catalytically active sites by exfoliation. On the one hand, complete structural exfoliation can spontaneously promote active site exposure at the surface of the

 This journal is © The Royal Society of Chemistry 2023

Open Access Article. Published on 20 kwietnia 2023. Downloaded on 29.01.2026 18:22:29.
This article is licensed under a Creative Commons Attribution-NonCommercial 3.0 Unported Licence.

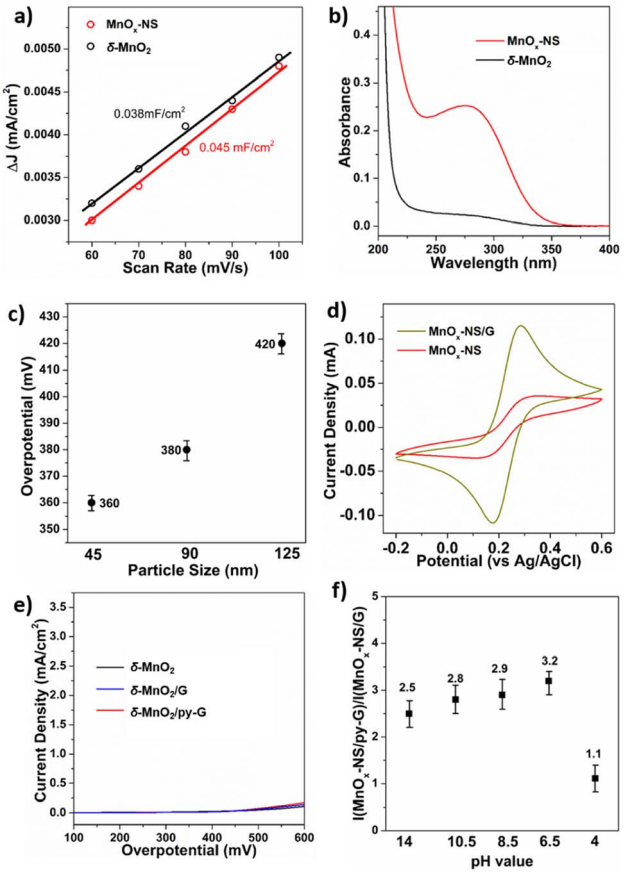

Fig. 3 (a) The ECSA measurement: ΔJ ($J_a - J_c$) from the CV curves of δ-MnO_2 and MnO_x-NS plotted against scan rates. (b) UV-vis absorption spectra of a 20 mM sodium pyrophosphate solution after dipping δ-MnO_2 and MnO_x-NS. (c) Comparison of the required overpotential for 0.5 mA cm^{-2} current density on MnO_x-NS with a particle size of 45, 90, and 125 nm. (d) CV curves of MnO_x-NS and MnO_x-NS/G in 0.1 M KCl electrolyte containing 10 mM $Fe(CN)_6^{3-/4-}$ ions. (e) LSV curves of δ-MnO_2, δ-MnO_2/G, and δ-MnO_2/py-G. (f) Comparison of I(MnO_x-NS/py-G)/I(MnO_x-NS/G) under pH 14, pH 10.5, pH 8.5, pH 6, and pH 4 conditions.

monolayer nanosheets. To verify this, Na^+ was introduced into the MnO_x-NS colloidal suspension to promote the self-reassembly of MnO_x-NS, regenerating layered δ-MnO_2.[20] The XRD pattern of the re-assembled sample presents a typical diffraction peak of a layered structure with an interlayer space of 0.73 nm, indicating the reformation of the layered δ-MnO_2 (Fig. S13a†). The electrocatalytic performance of this reformed δ-MnO_2 dramatically decreased compared with that of MnO_x-NS (Fig. S13b†). The remarkable activity difference between MnO_x-NS and δ-MnO_2 and our previous active "c-disordered" δ-MnO_x demonstrates the importance of the exposure of the MnO_2 nanosheet for efficient electrocatalytic water oxidation. However, we cannot exactly explain why δ-MnO_2 has the same charge transfer properties as MnO_x-NS, *i.e.*, the same ECSA, but the ordered MnO_2 nanosheet has deficient catalytic performance for water oxidation.

On the other hand, based on the TEM images, the average particle size of MnO_x-NS was estimated to be around 90 nm (Fig. S14†), which is much smaller than the 240 nm of δ-MnO_2. Without a well-ordered layered structure, the MnO_x monolayer will collapse and break, leading to a decrease in particle size. The formed smaller nanosheets promoted the exposure of coordinatively unsaturated edge- and corner-sites, which are believed to be involved in water oxidation as highly reactive catalytic sites.[44,49] To further verify this, MnO_x-NS with different lateral sizes were separated by controlled centrifugation, and denoted as MnO_x-45 and MnO_x-125 (Fig. S15†). A close relationship is presented between the lateral size and OER activity: where MnO_x-45 with a smaller particle size shows higher activity than MnO_x-90; whereas MnO_x-125 with a larger particle size displays lower activity compared with MnO_x-90 (Fig. 3c and S16†). These results demonstrate OER activity enhancement with particle size decrement. By the exfoliation process, plenty of coordinated unsaturated edge sites were generated on MnO_x-NS (Fig. S17†), which are much easier to be oxidized to high-valent key intermediate states for water oxidation.[14,47,48,50–53]

Effects of fast electron transfer

MnO_x-NS/G shows a 10 times higher activity compared with MnO_x-NS. LSV and long-term electrolysis were used to show that bare graphene displays minor water oxidation. This indicates that the graphene substrate promotes the catalytic system rather than introducing more active sites (Fig. S18†). Graphene serves as a loading substrate to promote the uniform distribution of MnO_x-NS with less stacking, as displayed in the XRD and TEM images of MnO_x-NS/G and MnO_x-NS/py-G (Fig. 1g and S19†). More importantly, the graphene substrate with excellent charge transportation capacity can facilitate electron transfer during the OER process.[54,55] To probe the enhancement in electron transfer by graphene, CV of $K_4Fe(CN)_6$ was performed using a MnO_x-NS and MnO_x-NS/G covered GC electrode as the working electrode. In contrast to the broad redox peak of Fe^{2+}/Fe^{3+} for MnO_x-NS/GC, a sharp Fe^{2+}/Fe^{3+} peak was observed in the CV curve measured with MnO_x-NS/G/GC (Fig. 3d). The promoted Fe^{2+}/Fe^{3+} redox couple on MnO_x-NS/G/GC illustrates that the combination of MnO_x-NS with graphene effectively solves the slow charge transfer problems. The lowered Tafel slopes can also demonstrate the acceleration of electron transfer after graphene introduction (Fig. S8†). The Tafel slopes were calculated to be 89 mV dec^{-1} and 86 mV dec^{-1} (approaching 60 mV dec^{-1}) for MnO_x-NS/G and MnO_x-NS/py-G, which are much smaller than the 134 mV dec^{-1} (~120 mV dec^{-1}) of pristine MnO_x-NS, indicating that the rate-determining step has been changed from the first electron transfer to the chemical reaction that takes place after the one-electron transfer,[48,56,57] demonstrating the improvement in catalytic kinetics.[44,47,58]

The synergy of active site exposure and fast electron transfer can be displayed by the catalytic performance of δ-MnO_2/G and δ-MnO_2/py-G. No noticeable activity enhancement was observed when δ-MnO_2 was assembled with graphene or py-graphene, indicating that the promoting effect of graphene requires optimal assembly between graphene and an exfoliated 2D nanosheet structure (Fig. 3e). These results demonstrate that the further 10-fold enhancement of the OER activity of MnO_x-

Open Access Article. Published on 20 kwietnia 2023. Downloaded on 29.01.2026 18:22:29.
This article is licensed under a Creative Commons Attribution-NonCommercial 3.0 Unported Licence.

NS/G compared with that of MnO_x-NS arises from the synergy of 3D → 2D structural exfoliation and fast electron transfer of graphene.

Effects of molecular pyridyl modification

It has been reported that introducing pyridine into electrolytes can prominently improve the catalytic performance of MnO_x electrocatalysts[17] and α-Fe_2O_3 photoanodes.[59] In these systems, pyridine can work as a proton transfer relay, facilitating the proton-coupled electron transfer in the catalytic process. For MnO_x-NS/py-G, we directly modified the graphene surface, *i.e.*, the catalytic environment, with a pyridyl molecule to accelerate proton transfer during water oxidation. The MnO_x-NS loading on graphene afforded a two-fold increase in activity. A pH dependence of OER activity was established to evaluate the proton transfer properties in the catalytic process (Fig. S20†). Fig. 3f shows the OER activities of MnO_x-NS/G and MnO_x-NS/py-G in electrolytes at different pH values (pH ranging from 4 to 14). In contrast to the significantly enhanced performance under pH ≥ 6.5 conditions, the pyridine modification shows minor enhancements in the OER at pH 4. The absence of increased activity at pH 4 can be attributed to the inhibited proton transfer relay effect of the pyridine group, which possesses a pK_a value around 5 and is thus mainly present as its conjugate acid. The deuterium kinetic isotope effect (KIE) was evaluated to study the role of proton transfer in the rate determining step (RDS). The KIE values of MnO_x-NS/py-G and MnO_x-NS/G were determined to be 3.4 and 4.3, respectively, which exhibit primary deuterium kinetic isotope effects, indicating that the rate-determining step (RDS) during water oxidation involves proton transfer. The lower KIE value of MnO_x-NS/py-G compared with that of MnO_x-NS/G illustrates the facilitated proton transfer by the introduced pyridyl functionality (Fig. S21†). These pH-dependence and KIE studies demonstrate the proton transfer relay effect of pyridine modification.[60,61]

The above analyses elucidate that the origin of the dramatically enhanced catalytic activity of *x*-NS/py-G is a combined result of 3D → 2D structural exfoliation, the graphene substrate, and pyridyl molecule modification. The 2D structure of MnO_x-NS achieved by exfoliation significantly increased the number of catalytically active sites in the MnO_x-NS/py-G catalyst. The nanocomposite structure between 2D MnO_x-NS and the graphene substrate provided a fast electron transfer pathway. And the pyridyl group modification accelerated proton transport during water oxidation. The synergy of catalytically active site exposure, fast electron transport, and efficient proton transport accounts for the increased activity by 600 times (Scheme 3), respectively contributing 30 times, 10 times, and 2 times to the overall activity enhancement (Fig. 2a and b). The clear revelation of the structure–activity relationship of the MnO_x-NS/py-G composites demonstrates the significance of the holistic functional biomimetic in electrocatalyst design, as the impact of each factor on the overall catalytic performance is multiplied.

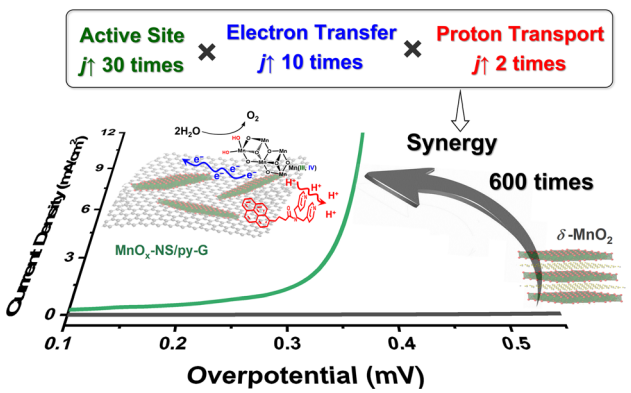

Scheme 3 Schematic illustration of the origin of the dramatic activity enhancement owing to the synergy of catalytically active site exposure, fast electron transport, and efficient proton transport.

Conclusions

A natural OEC catalyzes water oxidation with a low overpotential and high turnover frequency because it is an integrated system that realizes the synergy of water molecule activation, O–O bond formation, electron transfer, and proton transport. The design of water oxidation electrocatalysts need to follow nature's course, not only simulating the catalytic site structure but also creating an overall synergistic system. Starting from typical δ-MnO_2, we developed MnO_x-NS/py-G composites with a 600-fold activity improvement owing to the synergy of active site exposure, fast electron transport, and facilitated proton transport. Further studies indicate that the influence of each of the above factors on the overall catalytic performance is multiplied; therefore, outstanding activity can be achieved when the catalyst possesses efficient active sites, electron transfer, and proton transport simultaneously. In the development of water oxidation catalysts, in-depth analysis of factors leading to low catalytic activity can guide precise modification of the catalyst design for significantly improving the catalytic performance. This work demonstrates the success and significance of holistic functional biomimetics in electrocatalyst design, thereby providing a universal and *de novo* electrocatalyst design concept.

Author contributions

L. S., B. Z. and L. F. conceived and designed the idea. B. Z. and L. F. designed the experiments. L. F. collected and analyzed the data. Y. S., B. J. J. T., and A. K. assisted with the experiments and characterization. F. Z. carried out the AFM measurements. L. F. and B. Z. discussed the results and wrote the manuscript. L. S. revised the manuscript. All the authors reviewed and contributed to this paper.

Conflicts of interest

There are no conflicts to declare.

This journal is © The Royal Society of Chemistry 2023

Open Access Article. Published on 20 kwietnia 2023. Downloaded on 29.01.2026 18:22:29.
This article is licensed under a Creative Commons Attribution-NonCommercial 3.0 Unported Licence.

Acknowledgements

This paper is dedicated to Prof. Licheng Sun on his 60th birthday. We acknowledge the financial support of this work from the National Key R&D Program of China (2022YFC3401802), the Swedish Energy Agency, the Knut and Alice Wallenberg Foundation (KAW 2016.0072), the National Natural Science Foundation of China (22279105), the Kunpeng research fund from Zhejiang Province, the Research Center for Industries of The Future at Westlake University, and Zhejiang Laboratory for Energy and Carbon Neutralization. We sincerely thank Prof. Jinshan Pan at the KTH Royal Institute of Technology for assistance with the AFM measurements. We sincerely thank Prof. Xin Zhang at Westlake University for the discussions on the manuscript. L. Fan acknowledges financial support from the Swedish Research Council (Vetenskapsrådet) for an International Postdoc Fellowship (2021-00282).

Notes and references

1 T. Faunce, S. Styring, M. R. Wasielewski, G. W. Brudvig, A. W. Rutherford, J. Messinger, A. F. Lee, C. L. Hill, H. deGroot, M. Fontecave, D. R. MacFarlane, B. Hankamer, D. G. Nocera, D. M. Tiede, H. Dau, W. Hillier, L. Wang and R. Amal, *Energy Environ. Sci.*, 2013, **6**, 1074–1076.
2 B. Zhang and L. Sun, *Chem. Soc. Rev.*, 2019, **48**, 2216–2264.
3 D. J. Vinyard, G. M. Ananyev and G. C. Dismukes, *Annu. Rev. Biochem.*, 2013, **82**, 577–606.
4 L. Hammarström and S. Styring, *Energy Environ. Sci.*, 2011, **4**, 2379–2388.
5 S. Ye, C. Ding, R. Chen, F. Fan, P. Fu, H. Yin, X. Wang, Z. Wang, P. Du and C. Li, *J. Am. Chem. Soc.*, 2018, **140**, 3250–3256.
6 N. Cox, D. A. Pantazis, F. Neese and W. Lubitz, *Acc. Chem. Res.*, 2013, **46**, 1588–1596.
7 P. Garrido-Barros, C. Gimbert-Surinach, R. Matheu, X. Sala and A. Llobet, *Chem. Soc. Rev.*, 2017, **46**, 6088–6098.
8 B. Zhang and L. Sun, *J. Am. Chem. Soc.*, 2019, **141**, 5565–5580.
9 M. M. Najafpour, G. Renger, M. Holynska, A. N. Moghaddam, E. M. Aro, R. Carpentier, H. Nishihara, J. J. Eaton-Rye, J. R. Shen and S. I. Allakhverdiev, *Chem. Rev.*, 2016, **116**, 2886–2936.
10 S. Park, Y. H. Lee, S. Choi, H. Seo, M. Y. Lee, M. Balamurugan and K. T. Nam, *Energy Environ. Sci.*, 2020, **13**, 2310–2340.
11 M. Wiechen, M. M. Najafpour, S. I. Allakhverdiev and L. Spiccia, *Energy Environ. Sci.*, 2014, **7**, 2203–2212.
12 J. G. Metz, P. J. Nixon, M. Rogner, G. W. Brudvig and B. A. Diner, *Biochemistry*, 1989, **28**, 6960–6969.
13 R. Hussein, M. Ibrahim, A. Bhowmick, P. S. Simon, R. Chatterjee, L. Lassalle, M. Doyle, I. Bogacz, I. S. Kim, M. H. Cheah, S. Gul, C. de Lichtenberg, P. Chernev, C. C. Pham, I. D. Young, S. Carbajo, F. D. Fuller, R. Alonso-Mori, A. Batyuk, K. D. Sutherlin, A. S. Brewster, R. Bolotovsky, D. Mendez, J. M. Holton, N. W. Moriarty, P. D. Adams, U. Bergmann, N. K. Sauter, H. Dobbek, J. Messinger, A. Zouni, J. Kern, V. K. Yachandra and J. Yano, *Nat. Commun.*, 2021, **12**, 6531.
14 B. Zhang, Q. Daniel, L. Fan, T. Liu, Q. Meng and L. Sun, *iScience*, 2018, **4**, 144–152.
15 K. H. Cho, S. Park, H. Seo, S. Choi, M. Y. Lee, C. Ko and K. T. Nam, *Angew. Chem., Int. Ed.*, 2021, **60**, 4673–4681.
16 R. D. Britt, D. L. Suess and T. A. Stich, *Proc. Natl. Acad. Sci. U. S. A.*, 2015, **112**, 5265–5266.
17 A. Yamaguchi, R. Inuzuka, T. Takashima, T. Hayashi, K. Hashimoto and R. Nakamura, *Nat. Commun.*, 2014, **5**, 4256.
18 B. Ma, W. Hou, Y. Han, R. Sun and Z.-H. Liu, *Solid State Sci.*, 2008, **10**, 141–147.
19 Q. Feng, E.-H. Sun, K. Yanagisawa and N. Yamasaki, *J. Ceram. Soc. Jpn.*, 1997, **105**, 564–568.
20 X. Yang, Y. Makita, Z. Liu, K. Sakane and K. Ooi, *Chem. Mater.*, 2004, **16**, 5581–5588.
21 X. Liang, Z. Zhao, M. Zhu, F. Liu, L. Wang, H. Yin, G. Qiu, F. Cao, X. Liu and X. Feng, *Environ. Sci.: Nano*, 2017, **4**, 1656–1669.
22 G. Zhao, J. Li, X. Ren, J. Hu, W. Hu and X. Wang, *RSC Adv.*, 2013, **3**, 12909.
23 H.-Q. Wang, J. Chen, S.-J. Hu, X.-H. Zhang, X.-P. Fan, J. Du, Y.-G. Huang and Q.-Y. Li, *RSC Adv.*, 2015, **5**, 72495–72499.
24 H. Liu, Z. Hu, L. Tian, Y. Su, H. Ruan, L. Zhang and R. Hu, *Ceram. Int.*, 2016, **42**, 13519–13524.
25 H. Kim, A. Watthanaphanit and N. Saito, *RSC Adv.*, 2016, **6**, 2826–2834.
26 H. Zhu, Q. Liu, J. Liu, R. Li, H. Zhang, S. Hu and Z. Li, *Electrochim. Acta*, 2015, **178**, 758–766.
27 J. Kern, R. Chatterjee, I. D. Young, F. D. Fuller, L. Lassalle, M. Ibrahim, S. Gul, T. Fransson, A. S. Brewster, R. Alonso-Mori, R. Hussein, M. Zhang, L. Douthit, C. de Lichtenberg, M. H. Cheah, D. Shevela, J. Wersig, I. Seuffert, D. Sokaras, E. Pastor, C. Weninger, T. Kroll, R. G. Sierra, P. Aller, A. Butryn, A. M. Orville, M. Liang, A. Batyuk, J. E. Koglin, S. Carbajo, S. Boutet, N. W. Moriarty, J. M. Holton, H. Dobbek, P. D. Adams, U. Bergmann, N. K. Sauter, A. Zouni, J. Messinger, J. Yano and V. K. Yachandra, *Nature*, 2018, **563**, 421–425.
28 J. Zabel, R. R. Nair, A. Ott, T. Georgiou, A. K. Geim, K. S. Novoselov and C. Casiraghi, *Nano Lett.*, 2012, **12**, 617–621.
29 X. Y. Yan, X. L. Tong, Y. F. Zhang, X. D. Han, Y. Y. Wang, G. Q. Jin, Y. Qin and X. Y. Guo, *Chem. Commun.*, 2012, **48**, 1892–1894.
30 A. J. Lucio and S. K. Shaw, *J. Phys. Chem. C*, 2015, **119**, 12523–12530.
31 E. Lebegue, J. Agullo and D. Belanger, *ChemSusChem*, 2018, **11**, 219–228.
32 Q. Kang, L. Vernisse, R. C. Remsing, A. C. Thenuwara, S. L. Shumlas, I. G. McKendry, M. L. Klein, E. Borguet, M. J. Zdilla and D. R. Strongin, *J. Am. Chem. Soc.*, 2017, **139**, 1863–1870.
33 A. C. Thenuwara, E. B. Cerkez, S. L. Shumlas, N. H. Attanayake, I. G. McKendry, L. Frazer, E. Borguet, Q. Kang, R. C. Remsing, M. L. Klein, M. J. Zdilla and D. R. Strongin, *Angew. Chem., Int. Ed.*, 2016, **55**, 10381–10385.

Open Access Article. Published on 20 kwietnia 2023. Downloaded on 29.01.2026 18:22:29.
This article is licensed under a Creative Commons Attribution-NonCommercial 3.0 Unported Licence.

34 A. C. Thenuwara, S. L. Shumlas, N. H. Attanayake, Y. V. Aulin, I. G. McKendry, Q. Qiao, Y. Zhu, E. Borguet, M. J. Zdilla and D. R. Strongin, *ACS Catal.*, 2016, **6**, 7739–7743.

35 D. A. Vermaas, S. Bajracharya, B. B. Sales, M. Saakes, B. Hamelers and K. Nijmeijer, *Energy Environ. Sci.*, 2013, **6**, 643–651.

36 K. L. Pickrahn, S. W. Park, Y. Gorlin, H. B. R. Lee, T. F. Jaramillo and S. F. Bent, *Adv. Energy Mater.*, 2012, **2**, 1269–1277.

37 M. Fekete, R. K. Hocking, S. L. Y. Chang, C. Italiano, A. F. Patti, F. Arena and L. Spiccia, *Energy Environ. Sci.*, 2013, **6**, 2222–2232.

38 C. Walter, P. W. Menezes, S. Loos, H. Dau and M. Driess, *ChemSusChem*, 2018, **11**, 2554–2561.

39 Y. Meng, W. Song, H. Huang, Z. Ren, S. Y. Chen and S. L. Suib, *J. Am. Chem. Soc.*, 2014, **136**, 11452–11464.

40 Y. Gorlin and T. F. Jaramillo, *J. Am. Chem. Soc.*, 2010, **132**, 13612–13614.

41 K. L. Pickrahn, Y. Gorlin, L. C. Seitz, A. Garg, D. Nordlund, T. F. Jaramillo and S. F. Bent, *Phys. Chem. Chem. Phys.*, 2015, **17**, 14003–14011.

42 J. Knöppel, M. Möckl, D. E. López, K. Stojanovski, M. Bierling, T. Böhm, S. Thiele, M. Rzepka and S. Cherevko, *Nat. Commun.*, 2021, **12**, 2231.

43 J. Schröder, V. A. Mints, A. Bornet, E. Berner, M. F. Tovini, J. Quinson, G. K. H. Wiberg, F. Bizzotto, H. A. E. Sayed and M. Arenz, *JACS Au*, 2021, **1**, 247–251.

44 F. Song and X. Hu, *Nat. Commun.*, 2014, **5**, 4477.

45 Z. Morgan Chan, D. A. Kitchaev, J. Nelson Weker, C. Schnedermann, K. Lim, G. Ceder, W. Tumas, M. F. Toney and D. G. Nocera, *Proc. Natl. Acad. Sci. U. S. A.*, 2018, **115**, E5261–E5268.

46 T. Takashima, K. Hashimoto and R. Nakamura, *J. Am. Chem. Soc.*, 2012, **134**, 1519–1527.

47 B. Zhang, H. Chen, Q. Daniel, B. Philippe, F. Yu, M. Valvo, Y. Li, R. B. Ambre, P. Zhang, F. Li, H. Rensmo and L. Sun, *ACS Catal.*, 2017, **7**, 6311–6322.

48 K. Jin, H. Seo, T. Hayashi, M. Balamurugan, D. Jeong, Y. K. Go, J. S. Hong, K. H. Cho, H. Kakizaki, N. Bonnet-Mercier, M. G. Kim, S. H. Kim, R. Nakamura and K. T. Nam, *J. Am. Chem. Soc.*, 2017, **139**, 2277–2285.

49 L. Fan, B. Zhang, B. J. J. Timmer, N. V. R. A. Dharanipragada, X. Sheng, C.-W. Tai, F. Zhang, T. Liu, Q. Meng, A. K. Inge and L. Sun, *Nano Energy*, 2020, **72**, 104656.

50 B. Zhang, Y. Li, M. Valvo, L. Fan, Q. Daniel, P. Zhang, L. Wang and L. Sun, *ChemSusChem*, 2017, **10**, 4472–4478.

51 B. Zhang and L. Sun, *Dalton Trans.*, 2018, **47**, 14381–14387.

52 Z. N. Zahran, E. A. Mohamed and Y. Naruta, *ACS Catal.*, 2016, **6**, 4470–4476.

53 G. Mattioli, I. Zaharieva, H. Dau and L. Guidoni, *J. Am. Chem. Soc.*, 2015, **137**, 10254–10267.

54 P. Chen, K. Xu, T. Zhou, Y. Tong, J. Wu, H. Cheng, X. Lu, H. Ding, C. Wu and Y. Xie, *Angew. Chem., Int. Ed.*, 2016, **55**, 2488–2492.

55 X. Cui, P. Ren, D. Deng, J. Deng and X. Bao, *Energy Environ. Sci.*, 2016, **9**, 123–129.

56 N. T. Suen, S. F. Hung, Q. Quan, N. Zhang, Y. J. Xu and H. M. Chen, *Chem. Soc. Rev.*, 2017, **46**, 337–365.

57 V. S. Kale, U. Sim, J. Yang, K. Jin, S. I. Chae, W. J. Chang, A. K. Sinha, H. Ha, C. C. Hwang, J. An, H. K. Hong, Z. Lee, K. T. Nam and T. Hyeon, *Small*, 2017, **13**, 1603893.

58 H. Vrubel, T. Moehl, M. Gratzel and X. Hu, *Chem. Commun.*, 2013, **49**, 8985–8987.

59 T. Takashima, K. Ishikawa and H. Irie, *Chem. Commun.*, 2016, **52**, 14015–14018.

60 W. Li, F. Li, H. Yang, X. Wu, P. Zhang, Y. Shan and L. Sun, *Nat. Commun.*, 2019, **10**, 5074.

61 Y. Tanahashi, K. Takahashi, Y. Tsubonouchi, S. Nozawa, S. I. Adachi, M. Hirahara, E. A. Mohamed, Z. N. Zahran, K. Saito, T. Yui and M. Yagi, *Proc. Natl. Acad. Sci. U. S. A.*, 2021, **118**, e2113910118.

This journal is © The Royal Society of Chemistry 2023